









Cite this: *RSC Adv.*, 2024, 14, 38183

# Starch-assisted facile gel formation method for the synthesis of Fe–Mn binary oxide for the simultaneous removal of As(III) and As(V)<sup>†</sup>

Anwarul Azim, <sup>a</sup> Md. Minhajul Alam Khan, <sup>a</sup> Shawon Saha, <sup>a</sup> Hridoy Roy, <sup>b</sup> Akter Hossain Reaz, <sup>ac</sup> A. K. M. Atique Ullah <sup>ac</sup> and Shakhawat H. Firoz <sup>\*,a</sup>

Researchers have significantly focused on eco-friendly methods for nanomaterial synthesis to reduce the reliance on hazardous chemicals. In light of this, this study presents an eco-friendly, straightforward, alkali-free method for synthesizing iron–manganese (Fe–Mn) binary oxide (FMBO) and their single oxides by adopting a direct gel formation approach using starch. The synthesized materials were characterized through FTIR, FESEM, EDX, and XRD. Based on the characteristics of the synthesized materials, the probable formation mechanism of nanomaterials within the starch matrix *via* gel formation was comprehensively investigated. The presence of  $\text{MnO}_4^-$  resulted in faster gelation than  $\text{Fe}^{3+}$  owing to its stronger oxidizing properties, leading to a more robust gel network that could stabilize nucleation, control the growth of nanoparticles, and thereby reduce particle agglomeration. The synthesized materials were further employed for the adsorptive removal of arsenic, and the findings demonstrate that FMBO was much more effective than the individual oxides in simultaneously eliminating arsenic species (III and V) with an adsorption capacity of  $79 \text{ mg g}^{-1}$  for total arsenic ( $\text{As(III)} + \text{As(V)}$ ) owing to its nanostructure, surface characteristics, and synergistic effects of Fe and Mn oxides. Our observation suggests that Mn oxide pre-oxidizes  $\text{As(III)}$  to  $\text{As(V)}$ , which is then efficiently adsorbed by Fe oxide. This study underscores the potential of starch-based nanomaterials in developing efficient materials with enhanced properties.

Received 1st September 2024  
Accepted 18th November 2024

DOI: 10.1039/d4ra06319h

rsc.li/rsc-advances

## 1. Introduction

Contamination of groundwater by arsenic (As) is a significant environmental and health issue affecting millions of people around the world. Chronic exposure to low concentrations of arsenic has been linked to a wide range of severe health effects, including cancer of internal organs, skin and cardiovascular diseases, and neurological disorders.<sup>1</sup> These health concerns are most acute in areas where groundwater is a major source of drinking water. International organizations such as the World Health Organization (WHO) and the United Nations International Children's Emergency Fund (UNICEF) are actively involved in addressing the crucial concerns of arsenic contamination. However, arsenic contamination is a challenging issue that requires coordinated efforts from

governments, researchers, and communities. Researchers around the world continue to work tirelessly to ensure safe drinking water and mitigate the long-term health impacts of arsenic exposure.

To date, different approaches have been employed for arsenic removal, including reverse osmosis, adsorption, ion exchange, enhanced coagulation, membrane filtration, and electro-dialysis.<sup>2,3</sup> Adsorption is considered the most promising and effective because of its easy operation, high efficiency, and cost-effectiveness compared to other methods.<sup>4,5</sup> Adsorbents, such as metal oxide nanoparticles, zeolite, carbon-based materials, and clay minerals, have been used to remove As from water.<sup>5</sup> However, apart from metal oxide nanoparticles, most of these adsorbents are not very effective, even at low arsenic concentrations, and often produce harmful sludge.<sup>6</sup> Consequently, more research efforts have been directed toward metal oxide nanoparticles owing to their higher efficiency and lower risk of generating harmful byproducts.<sup>5,6</sup> Furthermore, two species of arsenic (As) are predominantly found in groundwater: arsenite [ $\text{As(III)}$ ] and arsenate [ $\text{As(V)}$ ]. Both the arsenic species are found in water as oxy-ions in organic and inorganic forms.<sup>3,6</sup> Adsorption by metal oxides is typically efficient only for  $\text{As(V)}$  but not for  $\text{As(III)}$ , which is more prevalent in natural water. Notably,  $\text{As(III)}$  possesses higher mobility and toxicity compared

<sup>a</sup>Department of Chemistry, Bangladesh University of Engineering and Technology (BUET), Dhaka-1000, Bangladesh. E-mail: shfiroz@chem.buet.ac.bd; Tel: +880 1730-713767

<sup>b</sup>Department of Chemical Engineering, Bangladesh University of Engineering and Technology (BUET), Bangladesh

<sup>c</sup>Department of Chemistry, Michigan State University, East Lansing, MI 48824, USA

<sup>†</sup> Electronic supplementary information (ESI) available. See DOI: <https://doi.org/10.1039/d4ra06319h>


with As(v). To improve the As(III) removal efficiency, it needs to be converted to As(v) through a pre-oxidation process. This conversion is typically achieved using oxidants like ozone, chlorine, and permanganate.<sup>6</sup> However, these oxidation methods are expensive and complex to operate. Thus, researchers are focusing on designing adsorbents that can perform both adsorption and oxidation. Instead of using single metal oxides, binary or bimetallic oxides that offer both properties are being developed. Various binary oxides have been utilized for arsenic removal, including Fe–Mn, Fe–Al, Fe–Ce, Zn–Ce, and Ti–Mn.<sup>7–11</sup> Among these, Fe–Mn binary oxide (FMBO) has shown the best efficiency and promising results in effectively adsorbing as well as oxidizing arsenic species. The two components of the binary oxides play different roles. Fe oxides dominate the adsorption process due to their higher affinity to As species, which allows them to form complexes on the surface and readily adsorb As. Meanwhile, Mn oxides can effectively oxidize As(III) to As(v).<sup>12–14</sup> These synergistic effects and dual functionality of FMBO enhance the arsenic removal capacity.

Numerous approaches have been employed for FMBO synthesis, including hydrothermal, sol–gel, and precipitation methods. Nowadays, to minimize the use of toxic substances in the synthesis procedure, facile green synthesis approaches are being developed using biomaterials. In this context, several studies have reported the synthesis of FMBO using biomaterials, including starch, tea extract, lignin, and egg white.<sup>14–17</sup> Of these, starch is the most convenient and prominent candidate for the synthesis of FMBO. Starch is a complex carbohydrate-based bio-polymer composed of amylose and amylopectin molecules, both of which are glucose units connected by glycosidic linkages. Due to its biodegradability, affordability, and safety, starch is well-studied as a reducing agent, capping agent, and template in various synthesis methods, facilitating the formation and stabilization of nanoparticles. When starch is heated in the presence of water, its granules absorb water and swell, disrupting the semi-crystalline structure and leading to the formation of a thick, viscous gel network, allowing it to serve as a potential gelling agent in gel-based synthesis.<sup>18–20</sup> Farhana *et al.* (2021) utilized this property of starch to synthesize magnetic Fe<sub>2</sub>O<sub>3</sub> via direct starch-assisted gel formation.<sup>19</sup> In addition, Hoque *et al.* (2019) explored the stabilization and capping properties of starch by synthesizing uniformly shaped Fe<sub>2</sub>O<sub>3</sub> nanorods.<sup>20</sup> The polymeric structure of starch forms a helical-shaped carbon matrix with multiple polyol groups, acting as a soft template for nanoparticles and helping prevent their aggregation.<sup>19</sup> Reports on the synthesis of FMBO using starch have been published by some research groups.<sup>14,21</sup> In all these reports, FMBO has been synthesized in a starch solution in the presence of NaOH as the precipitant. However, some studies have identified sodium residue as contamination in the final product when NaOH or Na<sub>2</sub>CO<sub>3</sub> is used as the precipitant. Research has shown that the existence of sodium impurities can adversely affect the performance of mixed metal oxide materials by obstructing their active sites or blocking their active planes.<sup>22–24</sup> Einaga *et al.* (2013) found that when NaHCO<sub>3</sub> is used in the synthesis of Mn<sub>x</sub>O<sub>y</sub>, an impure phase of Na<sub>2</sub>Mn<sub>5</sub>O<sub>10</sub> is

formed.<sup>22</sup> Mirzaei *et al.* (2003) found that the presence of Na impurities has a detrimental effect on the catalytic activity of CuMn<sub>2</sub>O<sub>4</sub>.<sup>23</sup> As the amount of Na impurity increases, the catalyst activity decreases significantly. In another report, Castañeda *et al.* (2018) found that Na impurities obstruct the active sites of the catalyst, resulting in a decline in its overall performance.<sup>24</sup> Interestingly, this study also discovered that the existence of impurities leads to a decrease in the surface area of the material. To solve these issues, researchers have used organic bases, such as tetramethyl ammonium hydroxide, and other quaternary ammonia bases, but these possess toxicity and require safety precautions.<sup>25,26</sup> Therefore, it is necessary to develop a method that does not require a base. For this reason, starch can serve as a viable alternative. As stated previously, starch may serve multiple roles during the synthesis process. An ecofriendly method can be adopted by solely utilizing starch for the synthesis of FMBO. Starch possesses the capacity to form a gel when heated with water. This gel-forming property of starch enables the development of a straightforward direct gel mediated synthesis of FMBO without a base. This method will facilitate the investigation of the growth mechanism of FMBO inside starch, which can also be useful for synthesizing other significant nanoparticles through this facile and environmentally sustainable approach.

Herein, we have developed a facile, green, and base-free synthesis route to fabricate FMBO using starch. The starch matrix provides space for the growth of nanomaterials and also helps avoid agglomeration during particle synthesis. Furthermore, the probable mechanism of nanoparticle formation within the starch matrix is discussed. The arsenic removal efficiency and mechanisms of the single oxides and binary oxides are compared.

## 2. Experimental methods

### 2.1. Materials

Iron(III) nitrate (Fe(NO<sub>3</sub>)<sub>3</sub>·9H<sub>2</sub>O; Merck, Germany), potassium permanganate (KMnO<sub>4</sub>; Merck, Spain), nitric acid (HNO<sub>3</sub>; 65%; Merck, Germany), starch (Scharlau, Spain), pH buffer capsules (Merck, Germany), sodium hydroxide pellets (NaOH; Merck, Germany), disodium hydrogen arsenate heptahydrate (Na<sub>2</sub>HAsO<sub>4</sub>·7H<sub>2</sub>O; Merck, Germany), and arsenic trioxide (As<sub>2</sub>O<sub>3</sub>; Sigma Aldrich, Germany) were purchased. All the chemicals were analytical grade and used without further purification. Deionized water (2 μs cm<sup>−1</sup>) was used for preparing the solutions needed for the experiments. DI water was obtained from a water purification system (Barnstead nano-pure, Thermo Scientific, USA).

### 2.2. Synthesis of nanoparticles

**2.2.1 Synthesis of Fe<sub>2</sub>O<sub>3</sub> nanoparticles.** Iron oxide (Fe<sub>2</sub>O<sub>3</sub>) nanoparticles were synthesized by a direct starch-assisted gel formation method using starch as the gelling agent. In brief, 5 g of Fe(NO<sub>3</sub>)<sub>3</sub>·9H<sub>2</sub>O was dissolved in 50 mL DI water to prepare a precursor solution. Using a burette, the precursor solution was gradually added dropwise to 200 mL of a 25% starch



solution. The mixture was then heated at 80 °C under constant stirring for several hours (~9 h) until a thick reddish-brown gel was formed. The obtained gel was left undisturbed for 24 h and then dried at 60 °C for 48 h in a hot air oven. The dried product was subsequently washed multiple times with DI water and then annealed at 650 °C for 4 h in a muffle furnace in the presence of air to form Fe<sub>2</sub>O<sub>3</sub> nanoparticles.

**2.2.2 Synthesis of MnO<sub>2</sub> nanoparticles.** The MnO<sub>2</sub> nanoparticles were prepared using the same procedure used for the preparation of Fe<sub>2</sub>O<sub>3</sub> nanoparticles, which included the reduction of KMnO<sub>4</sub> with starch. 5 g of KMnO<sub>4</sub> was dissolved in 50 mL of DI water. Afterwards, the solution was gradually added to 200 mL of a 25% starch solution using a burette, followed by heating and continuous stirring until gelation occurred. The obtained gel was left undisturbed for 24 h, then dried at 60 °C for 48 h and washed several times. Subsequently, the resultant product was annealed at 650 °C for 4 h, leading to the formation of MnO<sub>2</sub> nanoparticles.

**2.2.3 Synthesis of FMBOs.** The FMBOs were also prepared using the same procedure as the Fe<sub>2</sub>O<sub>3</sub> and MnO<sub>2</sub> nanoparticles. FMBO was prepared using Fe/Mn at a 1 : 2.55 molar ratio. This composition was selected *via* trial and error. In accordance with the ratio, pre-calculated quantities of Fe(NO<sub>3</sub>)<sub>3</sub>·9H<sub>2</sub>O and KMnO<sub>4</sub> were dissolved in 100 mL DI water under magnetic stirring. The prepared solution was then dropwise added to 200 mL of a 25% starch solution using a burette. Then the solution was continuously stirred for 80 °C until gel formation and left undisturbed for 24 h. Then it was dried at 60 °C for 48 h and subsequently washed with DI water. The product was annealed at 650 °C for 4 h (Fig. 1).

### 2.3. Characterization of prepared FMBO

The chemical functional groups of the nanoparticles were evaluated by Fourier Transform Infrared (FTIR) spectral analysis. The spectra were recorded between 4000–400 cm<sup>-1</sup> in the transmission mode of an FTIR spectrophotometer (FTIR-8400,

Shimadzu, Japan). The surface morphology and elemental composition of the prepared samples were analyzed using a field-emission scanning electron microscope (FESEM; JSM-7600F JEOL, Japan) fitted with an energy-dispersive X-ray spectrometer (EDX). The phase composition and crystallinity of the prepared samples were investigated using an X-ray diffractometer (XRD; Smartlab, Rigaku, Japan).

### 2.4. Surface charge analysis

The surface charge of a material can be analyzed using the point of zero charge (PZC) test, which determines the pH value at which the surface charge components are neutral under specified conditions like temperature, pressure, and aqueous solution composition.<sup>27,28</sup> According to the salt addition technique, equal amounts of the substrate were added to a series of solutions with consistent ionic strength but varying pH levels.<sup>29</sup> In this procedure, 0.2 g of the sample was mixed with 40 mL of a 0.1 M NaNO<sub>3</sub> solution placed in several 50 mL centrifuge tubes. The pH of these solutions was adjusted using 0.1 M HNO<sub>3</sub> and 0.1 M NaOH to 2, 4, 6, 7, 8, 10, and 12 (±0.1 pH units). The initial pH values (pH<sub>i</sub>) of the supernatant in each tube were recorded. The samples were then agitated at 200 rpm for 24 h using an orbital shaker (Stuart-SSL1). After allowing the samples to settle, the final pH values (pH<sub>f</sub>) of the supernatant were measured. The PZC was determined by plotting the change in pH (ΔpH = pH<sub>i</sub> – pH<sub>f</sub>) against pH<sub>i</sub>. This experiment was also conducted using a 0.05 M NaNO<sub>3</sub> solution. All experiments were repeated three times, and the average values were recorded.

### 2.5. Sorption experiments

The As(III) and As(V) adsorption characteristics of the FMBO adsorbent were studied using batch experiments at room temperature at an initial pH value of 7.00 ± 0.1. In brief, As<sub>2</sub>O<sub>3</sub> and Na<sub>2</sub>HAsO<sub>4</sub>·7H<sub>2</sub>O were used to prepare stock solutions of As(III) and As(V), respectively. Typically, 20 mg of adsorbent was added to a 50 mL tube containing 50 ppm of As(III) and As(V) in

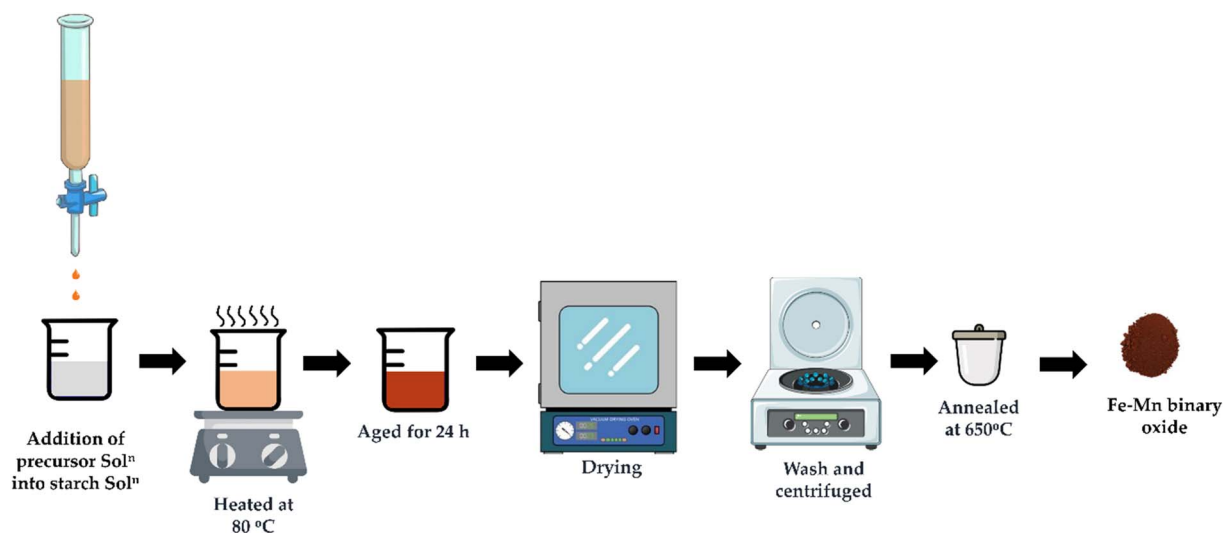


Fig. 1 Schematic of the synthesis of FMBO *via* the direct starch-assisted gel formation method.

solution. After adjusting the pH to about 7.0 using the buffer capsules, the mixture was agitated on an orbital shaker at 140 rpm for 24 hours while maintaining a temperature of 25 °C. After 24 hours, the equilibrium pH of the solution was determined, and the concentration of residual arsenic (As) in the solution was analyzed using an atomic absorption spectrometer (Varian AA280Z HGAAS, Australia) after filtration with a Whatman grade 40 ashless filter paper.

Initially, the absorbance values of standard solutions with known arsenic concentrations were measured, and a calibration curve was drawn by plotting the absorbance against concentration. Once the calibration curve was established, the absorbance of solutions with unknown arsenic concentrations was measured.

The concentration of the analyte was then calculated using the following formula.<sup>30</sup>

$$\text{Concentration (mg L}^{-1}\text{)} = \frac{\text{Absorbance}}{\text{Slope of the calibration curve}} \quad (1)$$

The amount of arsenic adsorbed at equilibrium ( $q_e$ ) and the removal efficiency ( $\eta$ ) for As(III), As(V) and As(III + V) were calculated using eqn (2) and (3), respectively.

$$q_e = \frac{V(C_0 - C_e)}{m} \quad (2)$$

$$\eta\% = \frac{C_0 - C_e}{C_0} \times 100\% \quad (3)$$

where  $C_0$  (mg L<sup>-1</sup>) and  $C_e$  (mg L<sup>-1</sup>) are the initial and equilibrium concentrations of As(III), As(V) and As(III + V), respectively.  $V$  (L) is the volume of the arsenic solution, and  $m$  (g) is the amount of used adsorbent. The batch adsorption tests were conducted in triplicate, and the average values were reported.

## 3. Results and discussion

### 3.1. Formation of starch-induced FMBO

**3.1.1. Characterization.** The comparative FTIR spectra of Fe<sub>2</sub>O<sub>3</sub>, MnO<sub>2</sub>, and the FMBO are illustrated in Fig. 2. The presence of broad peaks in the 3400–3600 cm<sup>-1</sup> region for all the synthesized products suggests the presence of intermolecular hydrogen bonding and stretching vibrations between the adsorbed water molecules, as shown in Fig. 2.<sup>31,32</sup> The presence of vibration frequencies at 2360 cm<sup>-1</sup>, 2362.8 cm<sup>-1</sup>, and 2361 cm<sup>-1</sup> is due to environmental CO<sub>2</sub>.<sup>33,34</sup> The absorption peak observed approximately at 1627 cm<sup>-1</sup>, 1635.6 cm<sup>-1</sup>, and 1653 cm<sup>-1</sup> are attributed to the asymmetric bending vibration of the C=O bond;<sup>35</sup> additionally, the strong peaks at 1056 cm<sup>-1</sup> and 1067 cm<sup>-1</sup> indicate the C–O stretching vibrations<sup>36</sup> likely due to the adsorption of monomeric glucose units from starch. In Fig. 2(a), the broad peaks at 556.48 cm<sup>-1</sup> and 466 cm<sup>-1</sup> indicate the Fe–O stretching vibration mode and the bending vibration mode of Fe<sub>2</sub>O<sub>3</sub>, respectively.<sup>37</sup> The bands at 595 cm<sup>-1</sup> and 528.51 cm<sup>-1</sup> are attributed to the valency vibrations and indicate the stability of the Mn–O bond.<sup>38</sup> In Fig. 2(c), a distinct peak is observed at 636.53 cm<sup>-1</sup>, which is characteristic of

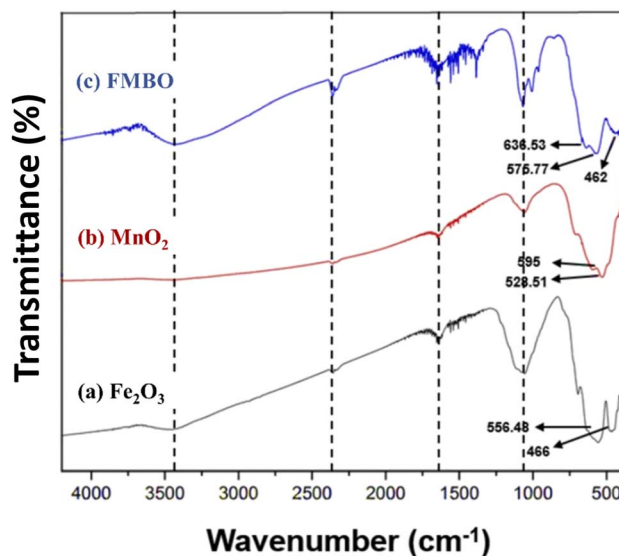


Fig. 2 The comparative FTIR spectra of (a) Fe<sub>2</sub>O<sub>3</sub>, (b) MnO<sub>2</sub>, and (c) FMBO.

MnO<sub>2</sub> and represents the Mn–O–Mn stretching vibration.<sup>39–41</sup> The peak observed at 575.77 cm<sup>-1</sup> represents the Fe–O stretching vibration, while the small shoulder peak observed at 462 cm<sup>-1</sup> corresponds to the Fe–O–Fe stretching vibration.<sup>42,43</sup> The peak at 807 cm<sup>-1</sup> in Fig. 2(c) may be due to the Fe–O–Mn structure,<sup>44</sup> which confirms the formation of the Fe–Mn binary oxide.

The XRD patterns of Fe<sub>2</sub>O<sub>3</sub>, MnO<sub>2</sub>, and FMBO nanoparticles are shown in Fig. 3. The diffraction peaks observed at  $2\theta = 33.1^\circ, 35.6^\circ, 49.5^\circ, 54.1^\circ, 57.5^\circ, 62.5^\circ$  and  $64.1^\circ$  in the XRD pattern of Fe<sub>2</sub>O<sub>3</sub> (COD database code: 9000139),<sup>45</sup> shown as a black line (a) in Fig. 3, reveals the hexagonal crystal structure of Fe<sub>2</sub>O<sub>3</sub>. The red line (b) in Fig. 3 illustrates the XRD pattern of MnO<sub>2</sub> (COD database code: 9016667),<sup>46</sup> and the diffraction peaks at  $2\theta = 28.6^\circ, 32.4^\circ, 36.1^\circ, 37.5^\circ, 41.9^\circ, 49.6^\circ, 56.2^\circ$  and  $59.9^\circ$  correspond to the tetragonal phase of MnO<sub>2</sub>. The diffraction peaks at  $2\theta = 30^\circ, 35.4^\circ, 43^\circ, 56.9^\circ$  and  $62.5^\circ$  in the XRD pattern of FMBO correspond to the Fe/Mn binary oxide Fe<sub>2</sub>MnO<sub>4</sub> (COD database code: 2300618),<sup>47</sup> as depicted in blue (c) in Fig. 3. The XRD of FMBO indicates the formation of a cubic Fe<sub>2</sub>MnO<sub>4</sub> structure, indicating a structural change with respect to individually prepared Fe<sub>2</sub>O<sub>3</sub> and MnO<sub>2</sub>. The crystal-size and lattice parameters of the synthesized materials were calculated using the Scherrer formula and Bragg's law from the base peaks and are summarized in Table S1.†

The morphology of the synthesized products was examined by FESEM. The FESEM image of Fe<sub>2</sub>O<sub>3</sub> illustrates the formation of nanoparticles with uniform orientation, as depicted in Fig. 4(a). The macromolecular structure of starch may possess the ability to suppress the overgrowth and agglomeration of nanoparticles by acting as a stabilizer, leading to uniformity in the shape and size of the particles.<sup>19</sup> Fig. 4(b) depicts that MnO<sub>2</sub> has a rod-like structure. When the binary oxide was prepared, the surface morphology underwent a complete change compared to the parent oxides. Fig. 4(c) reveals the formation of



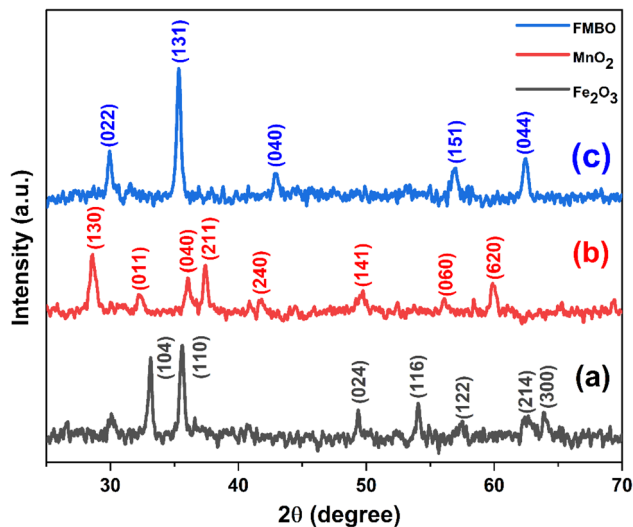


Fig. 3 XRD patterns of (a)  $\text{Fe}_2\text{O}_3$ , (b)  $\text{MnO}_2$ , and (c) FMBO.

cubic-shaped FMBO, with a porous network and an irregular and rough surface, which are favorable for efficient adsorption. The formation of pores after calcination at high temperatures is due to the decomposition of complex polymers into  $\text{CO}_2$  and water. As these molecules evaporate, they leave voids, leading to the creation of a porous and rough surface.

The elemental composition of the products was observed using EDX. The EDX analysis revealed the presence of carbon in all sample surfaces; due to high-temperature calcination, the starch decomposes, and carbon gets deposited on the surface, as shown in Table 1.

**3.1.2. The possible mechanism of starch-assisted FMBO formation.** Carbohydrates such as sucrose and glucose can control the growth, size, shape, and characteristics of nanoparticles. For instance, Sun *et al.*<sup>48</sup> utilized sucrose to regulate growth and precisely control the size of iron oxide nanoparticles. Hoque *et al.*<sup>20</sup> reported a straightforward technique for producing iron oxide nanoparticles at elevated temperatures by employing rice starch. Moreover, Ullah *et al.*<sup>49</sup> and Ali *et al.*<sup>50</sup> illustrated the precise regulation of manganese oxide NP formation utilizing starch and glycerol as reducing agents. Chen *et al.*<sup>51</sup> studied how glucose influences the better oxidation performance of FMBO and explained the tetracycline

Table 1 Elemental composition of the prepared samples based on EDS (weight%)

Materials	Fe%	Mn%	O%	C%
$\text{Fe}_2\text{O}_3$	9.60	—	16.01	74.39
$\text{MnO}_2$	—	17.84	16.23	65.93
FMBO	5.85	16.60	25.02	52.53

elimination process. However, the authors did not highlight the crucial aspect of the growth of FMBO in the presence of glucose, which is to be investigated. This will clarify how starch plays an important role in the formation of nanoparticles with regulated structures and inhibits aggregation. During the formation of nanoparticles assisted by starch, at the molecular level, the building units of starch interact with the metal ions to form a gel. Hence, it is essential to explore the atomic-level interactions of metal ions with the starch matrix to obtain a clear view of the starch-assisted gel formation technique.

In a previous study,<sup>20</sup> metal ions in salt solutions were mixed with a starch solution in alkaline conditions, leading to the hydrolysis of metal ions and the subsequent formation of metal hydroxides. These metal hydroxides interacted with starch, resulting in the formation of nanoparticles through hydrogen bond formation. However, in this work, aqueous solutions of potassium permanganate and ferric nitrate were gradually added to a starch solution at a preset concentration, unlike conventional methods that require the addition of alkali in the mixture. This method prevents the formation of metal hydroxides by allowing the metal salts to dissolve and directly form the corresponding ions in the aqueous starch solution. After that, the mixture was stirred vigorously at 80 °C till a gel was formed. The gel formation process involves a highly complex mechanism. Hence, this unexplored mechanism of forming binary metal oxides in a starch solution in the absence of an alkaline medium is an intriguing opportunity for a comprehensive investigation, contributing to the advancement of understanding in this field. Starch, being a polymer composed of interconnected glucose units, undergoes decomposition into smaller structures when heated to specific temperatures. The glucose monomers in starch are typically linked through C-1,4 or C-1,6 linkages, which contribute to the formation of the polymer. It is important to note that the  $\beta$ -C within each glucose

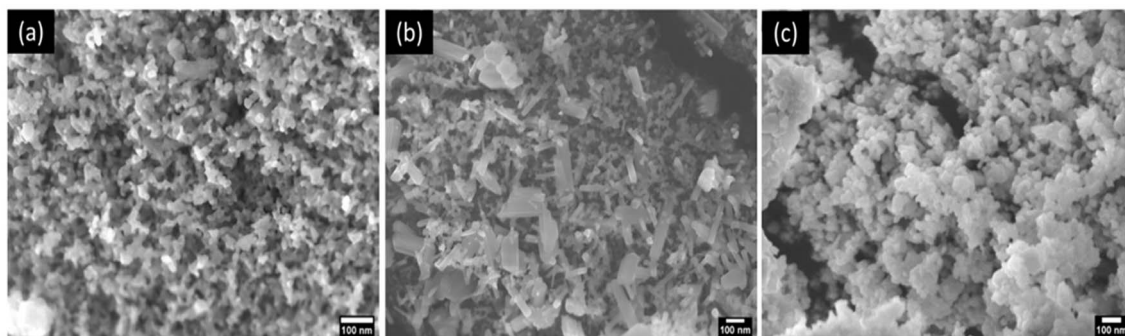
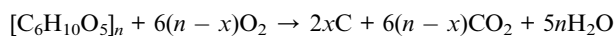
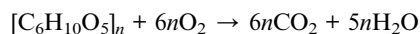


Fig. 4 FESEM images of (a)  $\text{Fe}_2\text{O}_3$ , (b)  $\text{MnO}_2$  and (c) FMBO.

unit is in close proximity to the carbonyl group present in the glucose molecule. Consequently, the oxygen atom in  $\beta$ -C becomes polarized and gains the ability to donate or share electrons with electron-deficient sites. Upon the dissolution of metal salts in the aqueous starch solution,  $\text{Fe}^{3+}$  and  $\text{MnO}_4^-$  ions are formed. The polarized oxygen groups present in the glucose units serve as electron-enriched centers, enabling the donation of electrons to metal cations, which act as electron-deficient centers. Consequently, a redox reaction takes place between the glucose units and metal cations, leading to the formation of a complex metal-glucose structure.

In our study, faster gelation was observed in the case of FMBO compared with iron oxide. This disparity can be attributed to the contrasting oxidizing properties of  $\text{Fe}^{3+}$  (a weak oxidizing agent) and  $\text{MnO}_4^-$  (a strong oxidizing agent). Slower gel formation with  $\text{Fe}^{3+}$  can be explained by the relatively slow rate of its redox reaction with glucose, whereas the rapid reduction of  $\text{MnO}_4^-$  leads to the quicker formation of a gel network. Additionally, it is possible that  $\text{MnO}_4^-$  interacts with oxygen units other than those present in  $\beta$ -C as it is a potent oxidizing agent, thereby contributing to the formation of a highly robust gel network. The gel network has a highly complex and cross-linked structure, which plays a crucial role in stabilizing nucleation and controlling the growth of nanoparticles. Specific metal ions assume distinct positions within the intricate network, leading to reduced particle agglomeration and enabling precise control of their shape and size.<sup>52,53</sup>

Subsequently, when the gel is calcined at a high temperature of approximately 650 °C, this complex polymeric structure undergoes decomposition by a combustion process, leading to the generation of carbon dioxide and water; moreover,  $\text{NO}_3^-$  from the salts is converted into  $\text{NO}_2$  and  $\text{O}_2$ , resulting in the formation of pores, voids and defects on the surface and thereby unlocking active sites, as shown in the following equations.<sup>50,53</sup>



During the calcination process, the generation of oxygen causes the formation of metal oxides, and their oxidation state may vary due to the presence of oxygen. These metal oxides remain in the form of binary oxides. In addition, the presence of starch plays an essential part in controlling the shape as well as textural properties of the composite.<sup>54</sup> A possible mechanism of the formation of binary oxide is shown schematically in Fig. 5.

Fig. 5 illustrates the formation of a highly complex metal-starch structure, leading to the formation of a gel. These interactions facilitate controlled nucleation and growth of the nanoparticles. Consequently, these interactions provide stable surface protection and passivation, preventing particle aggregation.<sup>55,56</sup>

Based on the above discussions, it can be inferred that in this study, FMBO was formed in a well-controlled manner. The FTIR analysis and XRD analysis also confirm the formation of the

binary oxide. The XRD analysis suggests that the synthesized FMBO possesses a uniform and compact crystalline structure. The presence of carbon in the synthesized product, as confirmed by the EDX analysis, is possibly due to the above-discussed reaction schemes.

### 3.2. Arsenic removal using FMBO

The removal of arsenic by the synthesized materials, namely  $\text{Fe}_2\text{O}_3$ ,  $\text{MnO}_2$ , and FMBO, was studied. The sorption capacity of  $\text{Fe}_2\text{O}_3$  for  $\text{As}(\text{v})$  was 5  $\text{mg g}^{-1}$ , while there was no sorption of  $\text{As}(\text{III})$ , and the sorption capacity for total arsenic ( $\text{As}(\text{III}) + \text{As}(\text{v})$ ) was found to be 2.5  $\text{mg g}^{-1}$ . The adsorption of  $\text{As}(\text{III})$  by  $\text{Fe}_2\text{O}_3$  is significantly challenging compared to  $\text{As}(\text{v})$  due to the distinct chemical characteristics of the two species.  $\text{As}(\text{III})$  predominantly exists in a charge-neutral form, especially in a neutral-pH solution. Since adsorption processes typically rely on electrostatic interactions between the adsorbent surface and the contaminant, the charge neutrality of  $\text{As}(\text{III})$  prevents any significant electrostatic attraction to the adsorbent. This lack of affinity complicates the adsorption process, which is further hindered by the high mobility and solubility of  $\text{As}(\text{III})$  in water. In contrast,  $\text{As}(\text{v})$  exists in a negatively charged form, enabling electrostatic affinity towards the adsorbent. Additionally,  $\text{As}(\text{v})$  is less mobile in water and hence is easy to adsorb.<sup>14</sup> As a result,  $\text{Fe}_2\text{O}_3$  was unable to adsorb  $\text{As}(\text{III})$ , while the adsorption of  $\text{As}(\text{v})$  was fairly possible. Moreover, the sorption study of  $\text{MnO}_2$  showed that it did not exhibit any sorption capacity for the arsenic species. It has been shown earlier that  $\text{MnO}_2$  can function as an oxidizing agent and converts  $\text{As}(\text{III})$  to  $\text{As}(\text{v})$ , while  $\text{Fe}_2\text{O}_3$  works as a potential adsorbent for  $\text{As}(\text{v})$ .

Consequently, the sorption capacity of FMBO for  $\text{As}(\text{III})$ ,  $\text{As}(\text{v})$ , and ( $\text{As}(\text{III}) + \text{As}(\text{v})$ ) was investigated by the same process. From Fig. 6(a), it is evident that FMBO had the highest sorption capacity for  $\text{As}(\text{III})$ ,  $\text{As}(\text{v})$  and ( $\text{As}(\text{III}) + \text{As}(\text{v})$ ). The sorption capacity of FMBO was found to be 15  $\text{mg g}^{-1}$ , 53  $\text{mg g}^{-1}$  and 79  $\text{mg g}^{-1}$  for  $\text{As}(\text{III})$ ,  $\text{As}(\text{v})$  and ( $\text{As}(\text{III}) + \text{As}(\text{v})$ ), respectively.

Fig. 6(b) illustrates the arsenic sorption efficacy of the nanomaterials towards arsenic removal from solutions containing  $\text{As}(\text{v})$ ,  $\text{As}(\text{III})$ , and ( $\text{As}(\text{III}) + \text{As}(\text{v})$ ), respectively. These findings highlight the potential of FMBO as an effective adsorbent for arsenic remediation. Table S2† provides information on the sorption capacity and sorption efficacy of  $\text{Fe}_2\text{O}_3$ ,  $\text{MnO}_2$  and FMBO for the removal of arsenic from solutions of  $\text{As}(\text{v})$ ,  $\text{As}(\text{III})$  and total arsenic, *i.e.* ( $\text{As}(\text{III}) + \text{As}(\text{v})$ ).

The surface charge of FMBO plays a crucial role in facilitating its high adsorption capacity for arsenic species, specifically  $\text{As}(\text{III})$  and  $\text{As}(\text{v})$ . This relationship is closely tied to the Point of Zero Charge (PZC) of the material. The isoelectric point of FMBO was found to be 9.01, as illustrated in Fig. S2.† PZC is a critical parameter that dictates the surface charge of FMBO under varying pH conditions. When the pH of the solution is below the PZC, the FMBO surface is positively charged due to the adsorption of excess protons. Conversely, when the pH exceeds the PZC, the surface charge turns negative.<sup>57</sup> In neutral aqueous media, FMBO remains positively charged because of



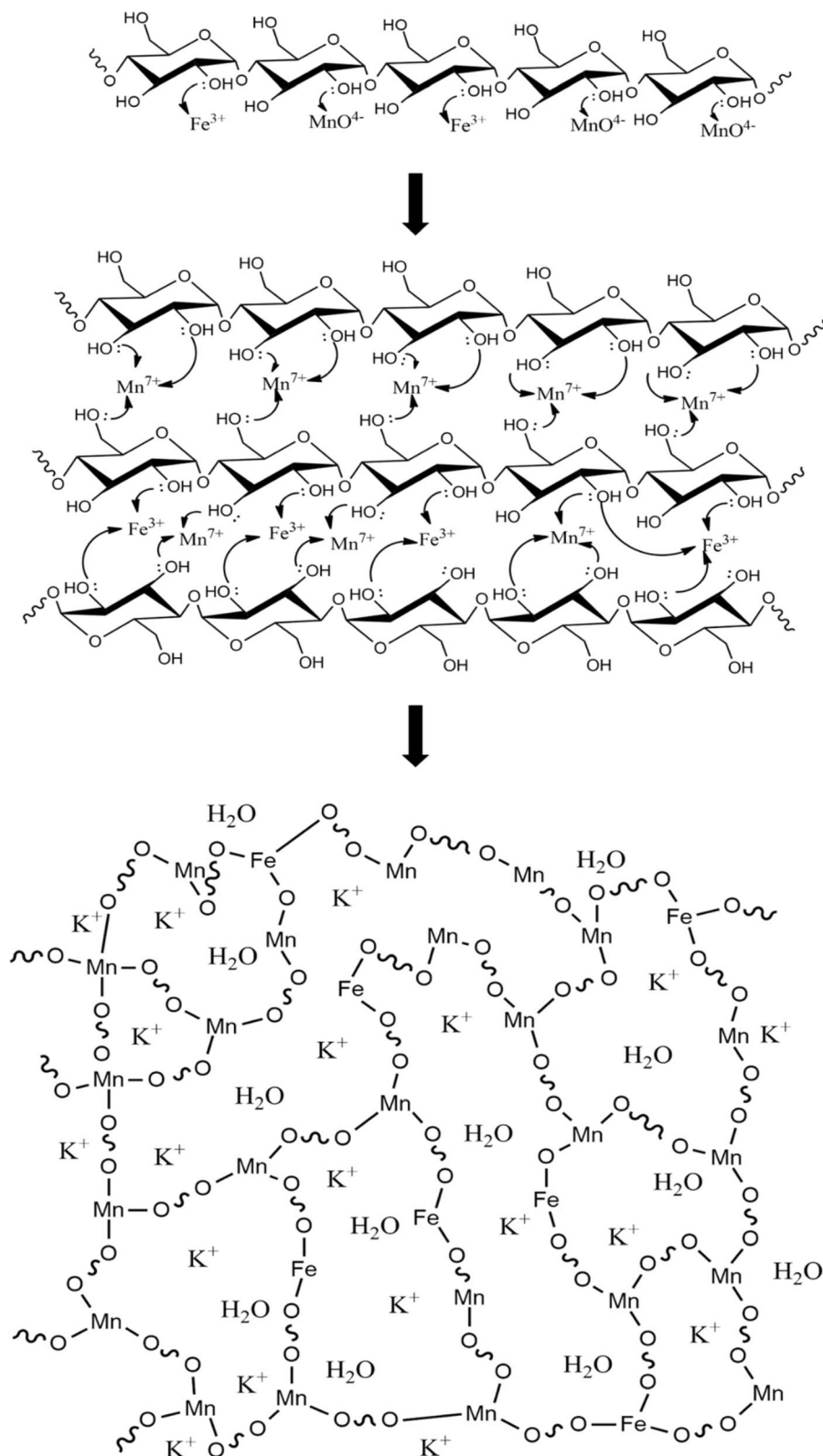


Fig. 5 Possible mechanism of the formation of FMBO within the starch matrix.

proton adsorption. This proton-rich surface can act as a Lewis acid.

In aqueous media,  $\text{As}(\text{v})$  primarily exists as negatively charged species, like  $\text{H}_2\text{AsO}_4^-$  and  $\text{HAsO}_4^{2-}$ . These anionic

species are effectively adsorbed onto the positively charged FMBO surface driven by coulombic interactions, resulting in its outstanding adsorption capability for  $\text{As}(\text{v})$ .

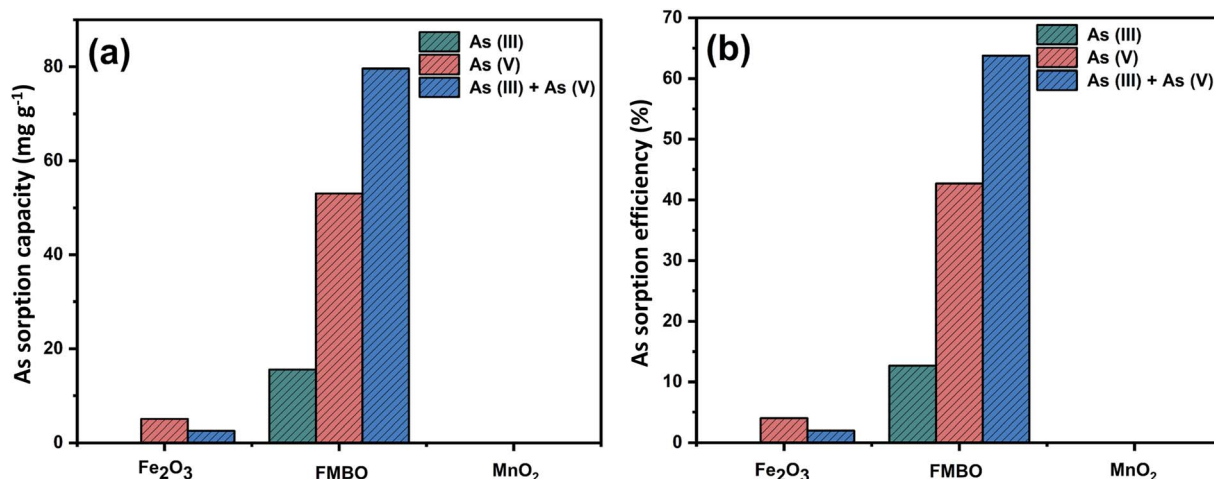
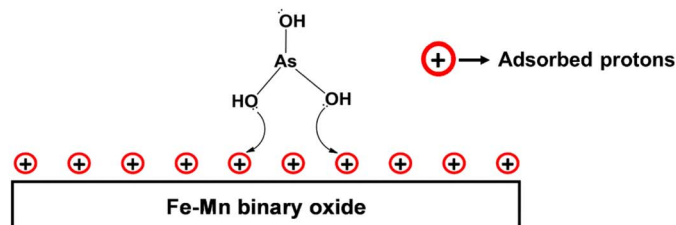


Fig. 6 Arsenic removal by Fe<sub>2</sub>O<sub>3</sub>, MnO<sub>2</sub>, and FMBO. (a) Sorption capacity of As(III), As(V), and (As(III) + As(V)). (b) Sorption efficiency of As(III), As(V) and (As(III) + As(V)).

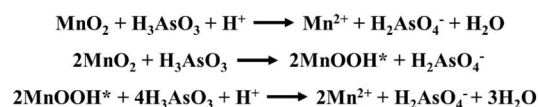
On the contrary, As(III) predominantly exists as the neutral or weakly charged species H<sub>3</sub>AsO<sub>3</sub> in aqueous media.<sup>58</sup> Due to the presence of lone pair electrons on the oxygen atoms, H<sub>3</sub>AsO<sub>3</sub> functions as a Lewis base. The interaction between the Lewis acidic FMBO surface and the Lewis basic As(III) facilitates the adsorption of As(III) onto FMBO.<sup>59</sup> Furthermore, As(III) undergoes oxidation to As(V) by donating electrons to Mn(IV) on the FMBO surface, resulting in the formation of As(V) oxyanions. The oxidation of As(III) to As(V) occurs *via* the sequential reduction of manganese; Mn(IV) is first reduced to Mn(III) and then from Mn(III) to Mn(II) *via* a two-step electron transfer

pathway.<sup>14,58</sup> Previous studies by Xiong *et al.*,<sup>60</sup> Ociński *et al.*<sup>61</sup> and Cao *et al.*<sup>62</sup> have explored the arsenic adsorption process, providing significant insights into the oxidation mechanism of As(III) to As(V) facilitated by manganese oxides through a two-step electron transfer pathway, as revealed by XPS analysis. During arsenic adsorption, MnO<sub>2</sub> in FMBO undergoes partial reduction to form MnOOH\*, indicating that MnO<sub>2</sub> accepts an electron, causing the reduction of Mn(IV) to Mn(III) in the first electron transfer step. As MnOOH\* accumulates, a subsequent electron transfer step reduces MnOOH\* further, forming the lower-valent Mn<sup>2+</sup> species. This progression from MnOOH\* to

#### Step-1: As (III) adsorbed by Lewis acid base interaction



#### Step-2: Oxidation of As (III) to As (V) by two step electron transfer mechanism



#### Step-3: As (V) adsorption by electrostatic interaction

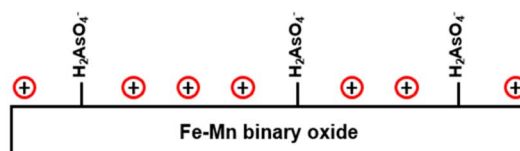


Fig. 7 Proposed mechanism for the removal of total arsenic from water using FMBO.



more further forms suggests a second electron transfer step. Following the two-step electron transfer pathway, As(III) oxidizes to produce As(V). These newly formed As(V) oxyanions are then adsorbed onto the FMBO surface through electrostatic interactions.

Another factor contributing to the superior adsorption performance of FMBO is the presence of carbon species on its surface, as revealed by the Energy-Dispersive X-ray Spectroscopy (EDX) analysis. It has been reported that carbon has a high adsorption capacity for arsenic.<sup>63</sup> The carbon matrix deposited on the FMBO surface during its synthesis from starch enhances the adsorption capacity through a synergistic effect, particularly for the simultaneous removal of As(III) and As(V).

The proposed mechanism of total arsenic removal from water using FMBO is schematically illustrated in Fig. 7.

From the above discussions, superior arsenic adsorption performance of FMBO can be attributed to several factors: (i) the positively charged surface of FMBO effectively interacts with arsenic species, facilitating their adsorption; (ii) MnO<sub>2</sub> present within FMBO acts as an oxidizing agent, converting neutral As(III) to negatively charged As(V); (iii) carbon deposited on the FMBO surface synergistically enhances the adsorptive properties of the material; and (iv) the porous nature of the surface and its activation by the formation of surface defects further improve the adsorption efficiency of the adsorbents.

## 4. Conclusions

A cost-effective and abundant biomaterial, starch, has been used in this work to develop a facile synthetic route for FMBO to achieve total arsenic removal from water. The starch matrix plays a crucial role in the growth of FMBO nanomaterials, leveraging its gel-forming property to stabilize nanoparticle growth and enhance its active surface area. Additionally, starch acts as a carbon source, improving the arsenic adsorption properties of the material. The As(III) and As(V) adsorption capacities of FMBO were higher than those of the individual oxides Fe<sub>2</sub>O<sub>3</sub> and MnO<sub>2</sub>, exhibiting an arsenic removal capacity of 79 mg g<sup>-1</sup>. This superior arsenic removal capacity is attributed to the synergistic effect of the binary oxide characteristics. To further understand this synergistic effect, the arsenic removal mechanism was explored, revealing that material composition, morphology and surface charge significantly influence the arsenic removal efficiency. This study opens a new route for the ecofriendly and green synthesis of nanomaterials with unique properties for various applications, including environmental remediation.

## Data availability

The data that support the conclusions of this research are included in the article and ESI†. Additional data that support the findings of this study are available from the corresponding author upon reasonable request.

## Conflicts of interest

The authors declare no conflict of interest.

## Acknowledgements

The authors would like to acknowledge the financial support from the Centre for Advanced Scientific Research (CASR), Bangladesh University of Engineering and Technology (BUET).

## References

- 1 P. L. Smedley and D. G. Kinniburgh, *Appl. Geochem.*, 2002, **17**, 517–568.
- 2 S. Alka, S. Shahir, N. Ibrahim, M. J. Ndejiko, D.-V. N. Vo and F. Abd Manan, *J. Cleaner Prod.*, 2021, **278**, 123805.
- 3 K. K. Sodhi, M. Kumar, P. K. Agrawal and D. K. Singh, *Environ. Technol. Innovation*, 2019, **16**, 100462.
- 4 R. E. C. Torrejos, G. M. Nisola, H. S. Song, L. A. Limjoco, C. P. Lawagon, K. J. Parohinog, S. Koo, J. W. Han and W.-J. Chung, *Chem. Eng. J.*, 2017, **326**, 921–933.
- 5 L. Hao, M. Liu, N. Wang and G. Li, *RSC Adv.*, 2018, **8**, 39545–39560.
- 6 S. I. Siddiqui and S. A. Chaudhry, *Process Saf. Environ. Prot.*, 2017, **111**, 592–626.
- 7 G. Zhang, F. Liu, H. Liu, J. Qu and R. Liu, *Environ. Sci. Technol.*, 2014, **48**, 10316–10322.
- 8 C. Meng, Q. Mao, L. Luo, J. Zhang, J. Wei, Y. Yang, M. Tan, Q. Peng, L. Tang and Y. Zhou, *Sep. Purif. Technol.*, 2018, **191**, 314–321.
- 9 U. K. Sahu, M. K. Sahu, S. S. Mohapatra and R. K. Patel, *J. Environ. Chem. Eng.*, 2016, **4**, 2892–2899.
- 10 A. Dhillon, S. K. Soni and D. Kumar, *J. Fluorine Chem.*, 2017, **199**, 67–76.
- 11 W. Zhang, C. Liu, T. Zheng, J. Ma, G. Zhang, G. Ren, L. Wang and Y. Liu, *J. Hazard. Mater.*, 2018, **353**, 410–420.
- 12 J. Li, H. Gyoten, A. Sonoda, Q. Feng and M. Xue, *RSC Adv.*, 2017, **7**, 1490–1497.
- 13 D. Nielsen-Franco and M. Ginder-Vogel, *ACS ES&T Water*, 2023, **3**, 1060–1070.
- 14 F. Xu, H. Chen, Y. Dai, S. Wu and X. Tang, *J. Environ. Manage.*, 2019, **245**, 160–167.
- 15 W. Chen, J. Wu, X. Weng, G. Owens and Z. Chen, *J. Cleaner Prod.*, 2022, **363**, 132406.
- 16 H. Yu, J. Yang, P. Shi, M. Li and J. Bian, *ACS Omega*, 2021, **6**, 16837–16846.
- 17 S. M. Hashemi, Z. Ataollahi, S. Hasani and A. Seifoddini, *J. Sol-Gel Sci. Technol.*, 2023, **106**, 23–36.
- 18 I. Uddin, S. M. Abzal, K. Kalyan, S. Janga, R. Patel and J. K. Dash, *J. Electron. Mater.*, 2023, **52**, 1710–1716.
- 19 F. Z. Farhana, M. Umer, A. Saeed, A. S. Pannu, M. Shahbazi, A. Jabur, H. J. Nam, K. Ostrikov, P. Sonar and S. H. Firoz, *ACS Appl. Nano Mater.*, 2021, **4**, 1175–1186.
- 20 M. I. U. Hoque, Y. Yamauchi, R. Naidu, R. Holze, R. Saidur, Q. Qu, M. M. Rahman, N. L. Torad, M. S. A. Hossain and M. Kim, *ChemistrySelect*, 2019, **4**, 3730–3736.



- 21 X. Yan, Y. Fei, L. Zhong and W. Wei, *Sci. Total Environ.*, 2020, **707**, 136064.
- 22 H. Einaga, N. Maeda and Y. Teraoka, *Appl. Catal., B*, 2013, **142**, 406–413.
- 23 A. A. Mirzaei, H. R. Shaterian, R. W. Joyner, M. Stockenhuber, S. H. Taylor and G. J. Hutchings, *Catal. Commun.*, 2003, **4**, 17–20.
- 24 R. Castañeda, L. Pascual and A. Martínez-Arias, *Catal. Commun.*, 2018, **108**, 88–92.
- 25 S. Ding, C. Zhu, H. Hojo and H. Einaga, *J. Hazard. Mater.*, 2022, **424**, 127523.
- 26 C. E. Shuck, K. Ventura-Martinez, A. Goad, S. Uzun, M. Shekhirev and Y. Gogotsi, *ACS Chem. Health Saf.*, 2021, **28**, 326–338.
- 27 M. Kosmulski, *Adv. Colloid Interface Sci.*, 2020, **275**, 102064.
- 28 I. A. Jasim, T. S. Mahmood, S. K. Al-Mamoori and L. A. Al-Maliki, *J. Urban Regen. Renew.*, 2021, **14**, 264–271.
- 29 T. Mahmood, M. T. Saddique, A. Naeem, P. Westerhoff, S. Mustafa and A. Alum, *Ind. Eng. Chem. Res.*, 2011, **50**, 10017–10023.
- 30 R. Islam, J. Al Foisal, M. Rahman, L. A. Lisa and D. K. Paul, *Afr. J. Environ. Sci. Technol.*, 2016, **10**, 9–17.
- 31 W. Liang, S. Wei, L. Lan, J. Chen, Y. Zhou, J. Zhao, H. Wang, R. Gao and F. Zeng, *RSC Adv.*, 2023, **13**, 24201–24210.
- 32 A. Tadjarodi, M. Imani and M. Salehi, *RSC Adv.*, 2015, **5**, 56145–56156.
- 33 B. Sun, Y. Wang, H. Bai, X. Liu, X. Li, L. Yang, H. Liu, X. Li and M. Wei, *Surf. Interfaces*, 2024, **49**, 104402.
- 34 M. Zhang, M. Wu, Z. Wang, R. Cheng, D. Y. Leung, Z. Lu and S. P. Feng, *Mater. Sci. Energy Technol.*, 2020, **3**, 734–741.
- 35 K. M. S. Meera, R. M. Sankar, J. Paul, S. N. Jaisankar and A. B. Mandal, *Phys. Chem. Chem. Phys.*, 2014, **16**, 9276–9288.
- 36 X. Chen, N. Yu, L. Zhang, Z. Liu, Z. Wang and Z. Chen, *RSC Adv.*, 2015, **5**, 96888–96895.
- 37 D. Kumar, H. Singh, S. Jouen, B. Hannoyer and S. Banerjee, *RSC Adv.*, 2015, **5**, 7138–7150.
- 38 M. Qin, H. Zhao, W. Yang, Y. Zhou and F. Li, *RSC Adv.*, 2016, **6**, 23905–23912.
- 39 R. Najjar, R. Awad and A. Abdel-Gaber, *J. Supercond. Novel Magn.*, 2019, **32**, 885–892.
- 40 J. Xu, Y.-Q. Deng, X.-M. Zhang, Y. Luo, W. Mao, X.-J. Yang, L. Ouyang, P. Tian and Y.-F. Han, *ACS Catal.*, 2014, **4**, 4106–4115.
- 41 W. E. Lee, R. Gadow, V. Mitic and N. Obradovic, *III Advanced Ceramics and Applications conference*, Springer, Serbia, 2016.
- 42 K. Song, W. Kim, C.-Y. Suh, D. Shin, K.-S. Ko and K. Ha, *Powder Technol.*, 2013, **246**, 572–574.
- 43 N. Chubar, V. Gerda, M. Szlachta and G. Yablokova, *Solid State Sci.*, 2021, **121**, 106752.
- 44 M. H. Habibi and V. Mosavi, *J. Mater. Sci.: Mater. Electron.*, 2017, **28**, 13643–13648.
- 45 R. Blake, R. Hessevick, T. Zoltai and L. W. Finger, *Am. Mineral.*, 1966, **51**, 123–129.
- 46 D. Taylar, *J. Therm. Expansion Data*, 1985, **84**, 181.
- 47 E. Solano, C. Frontera, T. Puig, X. Obradors, S. Ricart and J. Ros, *J. Appl. Crystallogr.*, 2014, **47**, 414–420.
- 48 X. Sun, C. Zheng, F. Zhang, Y. Yang, G. Wu, A. Yu and N. Guan, *J. Phys. Chem. C*, 2009, **113**, 16002–16008.
- 49 A. A. Ullah, A. F. Kibria, M. Akter, M. Khan, M. Maksud, R. A. Jahan and S. H. Firoz, *J. Saudi Chem. Soc.*, 2017, **21**, 830–836.
- 50 H. E. Ali, M. Abdel-Aziz, A. Aboraia, I. Yahia, H. Algarni, V. Butova, A. V. Soldatov and Y. Khairy, *Optik*, 2021, **227**, 165969.
- 51 Y. Chen, Z. Zeng, Y. Li, Y. Liu, Y. Chen, Y. Wu, J. Zhang, H. Li, R. Xu and S. Wang, *J. Colloid Interface Sci.*, 2020, **573**, 287–298.
- 52 S. Wintzheimer, T. Granath, M. Oppmann, T. Kister, T. Thai, T. Kraus, N. Vogel and K. Mandel, *ACS Nano*, 2018, **12**, 5093–5120.
- 53 A. K. Zak, W. A. Majid, M. Mahmoudian, M. Darroudi and R. Yousefi, *Adv. Powder Technol.*, 2013, **24**, 618–624.
- 54 W. Ojok, E. Ntambi, J. Bolender, J. Wasswa, W. Wanasolo and B. Moodley, *Carbohydr. Polym. Technol. Appl.*, 2022, **4**, 100241.
- 55 M. Á. Aguilar-Méndez, T. Espinosa-Solares, F. d. M. Guerrero-Toledo, D. Canseco-González, A. Velázquez-Hernández, G. S. Aguilar-Moreno and E. Navarro-Cerón, *IET Nanobiotechnol.*, 2020, **14**, 94–97.
- 56 H. Dong, Y. Cheng, Y. Lu, K. Hou, L. Zhang, L. Li, B. Wang, Y. Wang, Q. Ning and G. Zeng, *Sep. Purif. Technol.*, 2019, **210**, 504–510.
- 57 R. S. Bangari, V. K. Yadav, J. K. Singh and N. Sinha, *ACS Omega*, 2020, **5**, 10301–10314.
- 58 S. A. Baig, T. Sheng, Y. Hu, J. Xu and X. Xu, *Clean: Soil, Air, Water*, 2015, **43**, 13–26.
- 59 J. Chen, J. Wang, G. Zhang, Q. Wu and D. Wang, *Chem. Eng. J.*, 2018, **334**, 1518–1526.
- 60 Y. Xiong, Q. Tong, W. Shan, Z. Xing, Y. Wang, S. Wen and Z. Lou, *Appl. Surf. Sci.*, 2017, **416**, 618–627.
- 61 D. Ociński, I. Jacukowicz-Sobala, P. Mazur, J. Raczky and E. Kociolek-Balawejder, *Chem. Eng. J.*, 2016, **294**, 210–221.
- 62 C.-Y. Cao, J. Qu, W.-S. Yan, J.-F. Zhu, Z.-Y. Wu and W.-G. Song, *Langmuir*, 2012, **28**, 4573–4579.
- 63 D. Mohan and C. U. Pittman Jr, *J. Hazard. Mater.*, 2007, **142**, 1–53.

